crystals

MDPI

Article

Crystal Structure and Microwave Dielectric Characteristics of Novel $Ba(Eu_{1/5}Sm_{1/5}Nd_{1/5}Pr_{1/5}La_{1/5})_2Ti_4O_{12}$ High-Entropy Ceramic

Qing Wan [1,2], Zeping Li [1,2], Huifeng Wang [1,2], Gang Xiong [1,2] and Geng Wang [1,2,*]

[1] School of Electronic and Information Engineering, Hubei University of Science and Technology, Xianning 437100, China
[2] Key Laboratory of Photoelectric Sensing and Intelligent Control, Hubei University of Science and Technology, Xianning 437100, China
* Correspondence: wanggeng20001982@126.com

Abstract: High-permittivity $Ba(Eu_{1/5}Sm_{1/5}Nd_{1/5}Pr_{1/5}La_{1/5})_2Ti_4O_{12}$ (BESNPLT) high-entropy ceramics (HECs) were synthesized via a solid-state route. The microstructure, sintering behavior, phase structure, vibration modes, and microwave dielectric characteristics of the BESNPLT HECs were thoroughly investigated. The phase structure of the BESNPLT HECs was confirmed to be a single-phase orthorhombic tungsten-bronze-type structure of Pnma space group. Permittivity (ε_r) was primarily influenced by polarizability and relative density. The quality factor ($Q\times f$) exhibited a significant correlation with packing fraction, whereas the temperature coefficient (TCF) of the BESNPLT HECs closely depended on the tolerance factor and bond valence of B-site. The BESNPLT HECs sintered at 1400 °C, demonstrating high relative density (>97%) and optimum microwave dielectric characteristics with TCF = +38.9 ppm/°C, $Q\times f$ = 8069 GHz (@6.1 GHz), and ε_r = 87.26. This study indicates that high-entropy strategy was an efficient route in modifying the dielectric characteristics of tungsten-bronze-type microwave ceramics.

Keywords: microwave dielectric characteristics; tungsten-bronze-type ceramics; high-entropy ceramics; Raman spectroscopy

check for updates

Citation: Wan, Q.; Li, Z.; Wang, H.; Xiong, G.; Wang, G. Crystal Structure and Microwave Dielectric Characteristics of Novel $Ba(Eu_{1/5}Sm_{1/5}Nd_{1/5}Pr_{1/5}La_{1/5})_2Ti_4O_{12}$ High-Entropy Ceramic. *Crystals* **2024**, *14*, 754. https://doi.org/10.3390/cryst14090754

Academic Editor: Tomasz Sadowski

Received: 3 August 2024
Revised: 22 August 2024
Accepted: 23 August 2024
Published: 25 August 2024

1. Introduction

As vital materials for microwave transmission lines, oscillators, dielectric antennas, dielectric resonators, and filters utilized in wireless fidelity (WIFI), global positioning system (GPS), Bluetooth, wireless local area network (WLAN), and 5G/6G communication systems, microwave dielectric ceramics (MWDCs) have attracted sustained attention from researchers [1–5]. In these applications, the microwave dielectric characteristics of MWDC must be considered, including permittivity (ε_r), quality factor ($Q\times f$, $Q = 1/tan\delta$), and temperature coefficient (TCF or τ_f) [6–8]. In particular, a suitable ε_r is required, as well as a near-zero TCF and a high $Q\times f$ [9–11]. However, the simultaneous achievement of high ε_r, near-zero TCF, and high $Q\times f$ value represents a significant challenge in the field of MWDC.

Recently, the idea of high entropy was applied to functional ceramics, giving rise to the emergence of high-entropy ceramics (HECs) [12,13]. These new materials are single phase, comprising a minimum of five anions and/or cations occupying a single site within the crystal [14,15]. Extensive research has been conducted on HECs in order to enhance their properties [16]. HECs with low thermal conductivity [17], excellent mechanical properties [18], dielectric properties [19], piezoelectric properties [20], ferroelectric properties [21], and corrosion resistance [22] could be fabricated by precisely adjusting the composition within a wide range. These HECs have promising potential for various applications, including piezoelectricity [23], thermal barrier coatings [24], and energy storage [25]. Considering that dielectric properties of MWDC are highly sensitive to even the slightest alterations in structure and composition, high-entropy strategy might offer a novel methodology for tuning the dielectric characteristics. Xiang et al. [26] initially documented the finding of a high-entropy $Li(Lu_{0.2}Yb_{0.2}Er_{0.2}Ho_{0.2}Gd_{0.2})GeO_4$ MWDC with an orthorhombic olivine structure. Subsequently, numerous other high-entropy MWDC exhibiting optimal dielectric characteristics have been investigated [27–35]. Chen et al. [27] designed and synthesized $(Hf_{1/4}Zr_{1/4}Sn_{1/4}Ti_{1/4})O_2$ HECs, and $Q\times f$ increased significantly from 20,026 to 74,600 GHz by introduction of Hf^{4+} and Sn^{4+} into $ZrTiO_4$. According to Lin et al. [28], the TCF of $SrLaAlO_4$ MWDC could be adjusted from −32 to −6 ppm/°C via the introduction of equimolar Eu, Gd, Nd, and Sm in the La-site. Lai et al. [29] successfully synthesized non-equimolar $(Mg_{1/5}Co_{1/5}Ni_{1/5}Li_{2/5}Zn_{1/5})Al_2O_4$ HECs with TCF = −64 ppm/°C, $Q\times f$ = 58,200 GHz, and ε_r = 7.4. The above research mainly focuses on medium permittivity and ow-permittivity high-entropy MWDC, while there are scarce reports regarding high-entropy, high-permittivity, tungsten-bronze-type MWDC.

Previous investigations have demonstrated that $BaLa_2Ti_4O_{12}$ MWDC with a tungsten-bronze-type structure exhibits high permittivity (ε_r = 95.6) for miniaturized device applications. However, low-$Q\times f$ value (2102 GHz) and high-positive TCF (+352 ppm/°C) restrict its practical application [36]. Inspired by the concept of high entropy, the equimolar Eu^{3+}, Sm^{3+}, Nd^{3+}, and Pr^{3+} cations were incorporated into the A1-site (La-site) of $BaLa_2Ti_4O_{12}$ MWDC, forming HECs (with the nominal composition $Ba(Eu_{1/5}Sm_{1/5}Nd_{1/5}Pr_{1/5}La_{1/5})_2Ti_4O_{12}$ to improve the $Q\times f$ and temperature stability. In this work, $Ba(Eu_{1/5}Sm_{1/5}Nd_{1/5}Pr_{1/5}La_{1/5})_2Ti_4O_{12}$ (abbreviated as BESNPLT) HECs were fabricated through a solid-state route, and the microstructure, sintering behavior, phase structure, vibration modes, and microwave dielectric characteristics of the BESNPLT HECs were thoroughly investigated. The polarizability per molar volume (α_{the}/V_m), packing fraction (P.F.), tolerance factor (t), and B-site bond valence (V_B) were analyzed to determine the relationship between the microwave dielectric characteristics of the BESNPLT HECs.

2. Materials and Methods

$Ba(Eu_{1/5}Sm_{1/5}Nd_{1/5}Pr_{1/5}La_{1/5})_2Ti_4O_{12}$ HECs were synthesized through a solid-state route utilizing Eu_2O_3 (99.99%), Nd_2O_3 (99.99%), Pr_6O_{11} (99.9%), Sm_2O_3 (99.99%), La_2O_3 (99.99%), $BaCO_3$ (99.8%), and TiO_2 (99.84%). To remove moisture from the powders, Pr_6O_{11} was calcined for three hours at 600 °C, while Eu_2O_3, Nd_2O_3, La_2O_3, and Sm_2O_3 were calcined for the same period at 900 °C. The initial oxide and carbonate were weighed in accordance with the stoichiometry of $Ba(Eu_{1/5}Sm_{1/5}Nd_{1/5}Pr_{1/5}La_{1/5})_2Ti_4O_{12}$ (BESNPLT) and then were wet-milled in nylon jars (with deionized water and ZrO_2 balls) using a speed of 280 rpm for 2 h. The mixed powders were dried at 120 °C/8 h and calcined at 1175 °C/3 h to synthesize BESNPLT powder. Following calcination, the BESNPLT powder was subjected to a second wet-milling process and subsequently dried at 120 °C/8 h. The BESNPLT powder was combined with PVA (10 wt %) and pressed into cylindrical billets and flake billets. Finally, the BLPNSET billets (cylindrical and flake) were sintered at 1350–1500 °C/4 h.

The bulk density of the BESNPLT HECs was measured by the Archimedean drainage method. The phase structure of the BESNPLT ceramic was determined utilizing a BRUKER X-ray diffraction (XRD, USA, D8 advance), which has a detection range of 10°–90°. The evaluation of the natural, sintered surface of the BESNPLT ceramic specimens was conducted employing a ZEISS Scanning Electron Microscope (SEM, GEMINI300). The element distribution of the ceramic specimens was implemented via the utilization of an energy dispersive spectrometer (EDS, Oxford, X-MAX 50, UK). Raman spectra (50~850 cm^{-1}) of the BESNPLT HECs were obtained using a Alpha300R Raman scattering spectrometer (WITec, λ = 532 nm). Microwave dielectric characteristics of the BESNPLT HECs were evaluated at 5–6 GHz utilizing a P9375A network analyzer (USA, 0.3 MHz–26.5 GHz, Keysight) through the application of the Hakki–Coleman method [37]. The temperature coefficient (TCF) was determined using Equation (1):

$$\mathrm{TCF} = \frac{(f_{90} - f_{30}) \times 10^6}{(90 - 30) f_{30}} (\mathrm{ppm}/^\circ\mathrm{C}) \tag{1}$$

where f_{90} and f_{30} represent the resonant frequency at 90 °C and 30 °C, respectively.

3. Results and Discussion

The XRD patterns of the BESNPLT HECs sintered at varying temperatures (1350–1500 °C) are recorded in Figure 1. BESNPLT HECs consist of Sm^{3+} (1.079 Å), Eu^{3+} (1.066 Å), Pr^{3+} (1.126 Å), Nd^{3+} (1.109 Å), and La^{3+} (1.16 Å) in equal molar ratios, and its average ionic radius of lanthanide elements (1.108 Å) is close to that of Nd^{3+} (1.109 Å) [38]. It is, therefore, anticipated that the positions of the diffraction peaks will align closely with those of $BaNd_2Ti_4O_{12}$, as illustrated in Figure 1. The observed diffraction peaks of the BESNPLT specimens align with $BaNd_2Ti_4O_{12}$ (PDF#44–0061), and no additional peaks are detected, indicating that the BESNPLT HECs form an orthorhombic tungsten-bronze-type phase with Pnma space group.

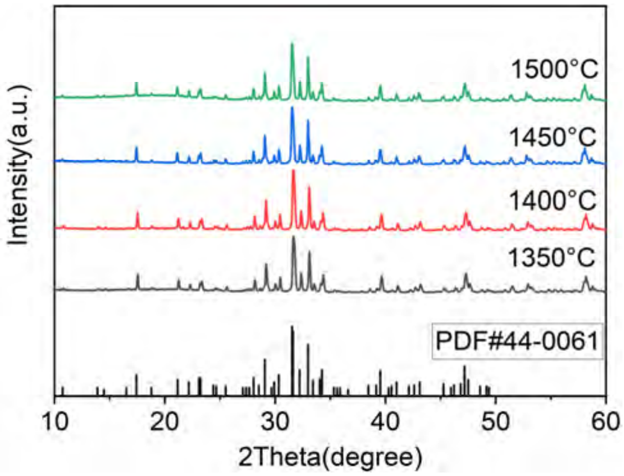

Figure 1. XRD patterns of BESNPLT HECs sintered at 1350–1500 °C.

To gain a comprehensive insight into the structural characteristics of the BESNPLT HECs, Rietveld refinements were conducted utilizing GSAS application [39,40], with the XRD data (2θ = 10–90°) obtained from BESNPLT specimens that had been sintered at 1400 °C. The homotopic $Ba_{4.5}Nd_9Ti_{18}O_{54}$ structure (ICSD # 95269) is employed in an initial model [41], and corresponding refined results for BESNPLT HECs are illustrated in Figure 2a and Table 1. There was satisfactory concordance between the fitted (black solid line) and observed patterns (red dot) with low values of R_p = 7.29%, R_{wp} = 9.18%, and χ^2 = 2.015 (Figure 2a and Table 1). The calculated cell volume (V) of the BESNPLT HECs sintered at 1400 °C is 2100.788 $Å^3$ (a = 22.3607 Å, b = 7.6992 Å, c = 12.2024 Å). Figure 2b presents a structural diagram of the BESNPLT HECs projected along [001]. As depicted in Figure 2b, tungsten-bronze-type BESNPLT HECs comprises a three-dimensional framework of a vertex-sharing Ti-O octahedron interconnected at the vertices to yield three distinct types of cavities: small triangular cavities (C), diamond cavities (A1), and pentagonal cavities (A2) [42]. The small triangular cavities (C-site) are empty. The Ba^{2+} cations occupy the large pentagonal cavities (A2-site), whereas the remaining Ba^{2+} ions are distributed among the diamond cavities (A1-site), sharing these with the lanthanides (Sm^{3+}, Eu^{3+}, Pr^{3+}, Nd^{3+}, and La^{3+}).

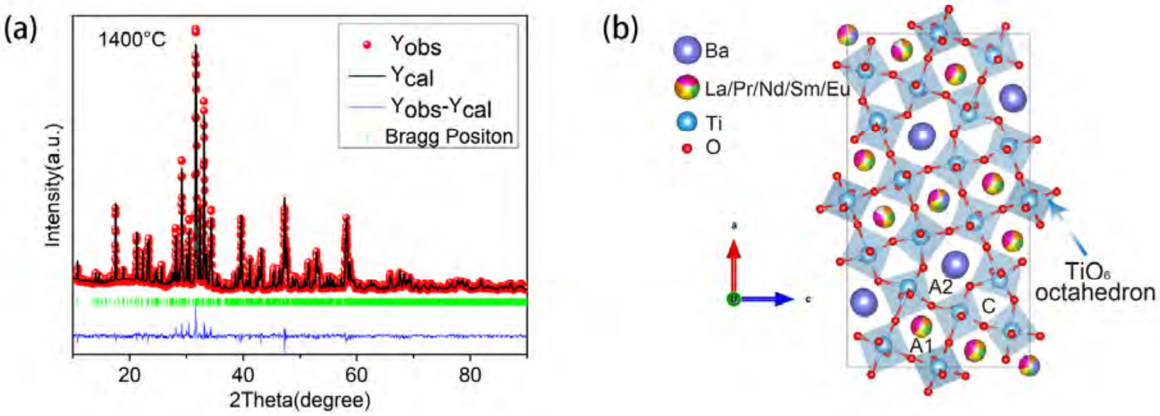

Figure 2. (**a**) Rietveld refinement plots of BESNPLT HECs. (**b**) Structural diagram of BESNPLT HECs.

Table 1. The refinement parameters of BESNPLT HECs.

BLPNSET	1350 °C	1400 °C	1450 °C	1500 °C
a (Å)	22.3557	22.3607	22.3667	22.3747
b (Å)	7.7011	7.6992	7.7009	7.7005
c (Å)	12.2031	12.2024	12.2048	12.2061
V (Å^3)	2100.934	2100.788	2102.217	2103.079
$\alpha = \beta = \gamma$	90	90	90	90
R_p (%)	6.65	7.29	7.33	6.92
R_{wp} (%)	8.48	9.18	9.44	8.96
χ^2 (%)	1.739	2.015	2.05	2.19
ρ_{theo} (g/cm^3)	5.7559	5.7563	5.7524	5.7501

Raman spectroscopy represents an effective methodology for the reflection of phase structural characteristics, cation distribution, and the identification of the defects of MWDC through the detection of bond vibration characteristics [43]. The theoretically Raman-active modes of $Ba_{4.5}Nd_9Ti_{18}O_{54}$ with a Pnma space group are 258 ($\Gamma_{Raman} = 73A_g + 56B_{1g} + 73B_{2g} + 56B_{3g}$). BESNPLT HECs with an identical space group (Pnma) also exhibit analogous Raman-active modes. However, the actual measurement of Raman-active modes was found to be less than the theoretical value, which was influenced by a number of factors, including peak overlap, background, and low intensity [44,45]. The Raman spectra (50 cm^{-1} ~ 850 cm^{-1}) of the BESNPLT HECs at varying temperatures (1350–1500 °C) are illustrated in Figure 3, and 13 Raman-active modes (around 80, 115, 133, 181, 231, 279, 298, 330, 404, 432, 530, 592, and 751 cm^{-1}, respectively) can be identified. As illustrated in Figure 3, the Raman-active modes remained largely unaltered with increased temperature, demonstrating that the structure of the BESNPLT HECs remained stable within the sintering temperature (S.T.) range. The Raman-active modes (80, 115, 133, and 181 cm^{-1}) within 50–200 cm^{-1} are associated with the A1 and A2-site cation (Ba^{2+}, Sm^{3+}, Eu^{3+}, Pr^{3+}, Nd^{3+}, and La^{3+}) translation of the BESNPLT HECs [46]. The modes (231, 279, 298, and 330 cm^{-1}) within the 200–400 cm^{-1} are derived from the rotation and tilt of titanium–oxygen (Ti-O) octahedron [47]. The Raman-active modes at 404 and 432 cm^{-1} are ascribed to bending the vibration of the titanium–oxygen bond [48]. The modes at 530 (A_g) and 592 cm^{-1} (B_{1g}) have been identified as stretching the vibration of the titanium–oxygen bond. The Raman-active mode at 751 cm^{-1} shows a correlation with second-order scattering [49]. Furthermore, Raman spectroscopic analysis has confirmed the formation of tungsten-bronze-type BESNPLT HECs.

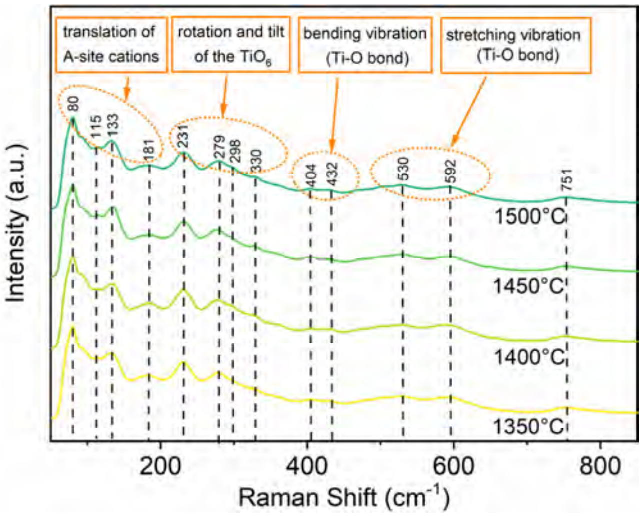

Figure 3. Raman spectra of BESNPLT HECs sintered at varying temperatures.

Figure 4 exhibits the relative density (ρ_{re}) and bulk density (ρ_{bu}) of the BESNPLT HECs at varying temperatures (1350–1500 °C). The ρ_{re} of the BESNPLT HECs could be evaluated through Equation (2):

$$\rho_{re} = \frac{\rho_{bu}}{\rho_{th}} \times 100\% \tag{2}$$

where ρ_{re} represents the theoretical density, with the value calculated using XRD refinement data presented in Table 1. As the S.T. increases, the ρ_{bu} of the BESNPLT HECs increases, achieving a maximum of 5.603 g/cm^3 at 1400 °C (97.34% of the theoretical value of 5.756 g/cm^3). Thereafter, the ρ_{bu} decreases as the S.T. exceeds 1400 °C.

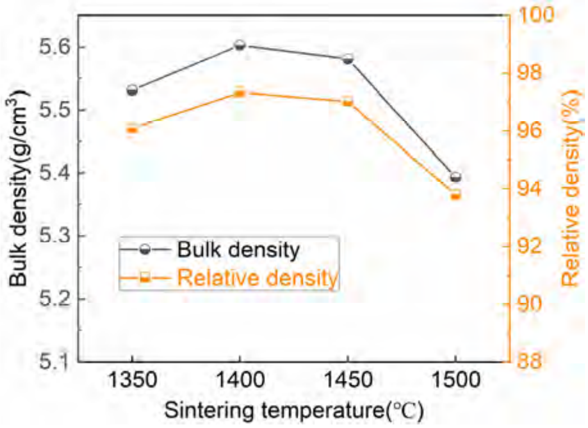

Figure 4. ρ_{re} and ρ_{bu} of BESNPLT HECs sintered at 1350–1500 °C.

SEM photographs of the as-fired BESNPLT HECs at varying temperatures (1350–1500 °C) are represented in Figure 5a–d. The grains of the BESNPLT HECs were observed to exhibit a rod-like morphology that was in accordance with the known characteristics of tungsten-bronze-type $Ba_{6\text{-}3x}R_{8+2x}Ti_{18}O_{54}$ (BRT, R = Sm, Nd, La, and Pr) ceramics [46–49]. As the S.T. rises, the average grain size of the BESNPLT HECs increases markedly as a consequence of grain growth. The formation of the uniform and dense (ρ_{re} > 95%) surface morphology of the BESNPLT HECs (see Figure 5a–c) was observed at 1350–1450 °C. Nevertheless, a further increase in the S.T. caused the formation of abnormal grains, characterized by the presence of pores (see Figure 5d). As illustrated in Figure 6, the EDS mapping demonstrates a highly uniform distribution of Sm^{3+}, Eu^{3+}, Pr^{3+}, Nd^{3+}, and La^{3+}, indicating that the lanthanide ions have succeeded in entering the A1-site in the crystal lattice. According to the EDS analysis results, the barium, titanium, oxygen, and lanthanide elements were consistent with the stoichiometry of the BESNPLT HECs, and the contents of the lanthanide elements (Eu^{3+}, Sm^{3+}, Nd^{3+}, Pr^{3+}, and La^{3+}) could be regarded as approaching equimolar proportions, with a ratio of 1.97:2.06:2.1:2.03:2.03. Consistent with the XRD and Raman analysis results, the EDS analysis also confirms the formation of the BESNPLT HEC's solid solution.

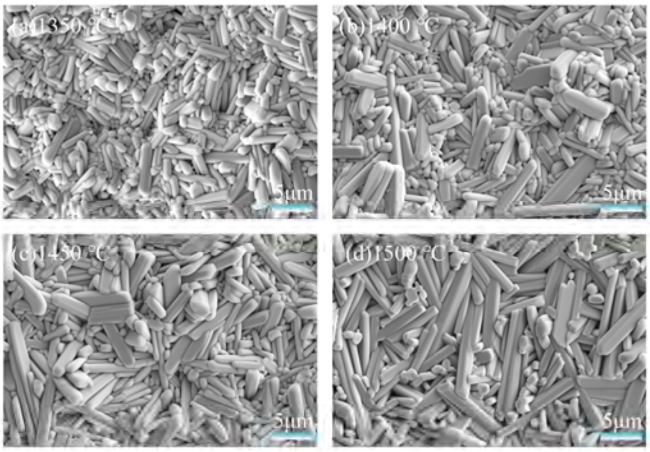

Figure 5. SEM morphology of BESNPLT HECs sintered at (**a**) 1350 °C; (**b**) 1400 °C; (**c**) 1450 °C; (**d**) 1500 °C.

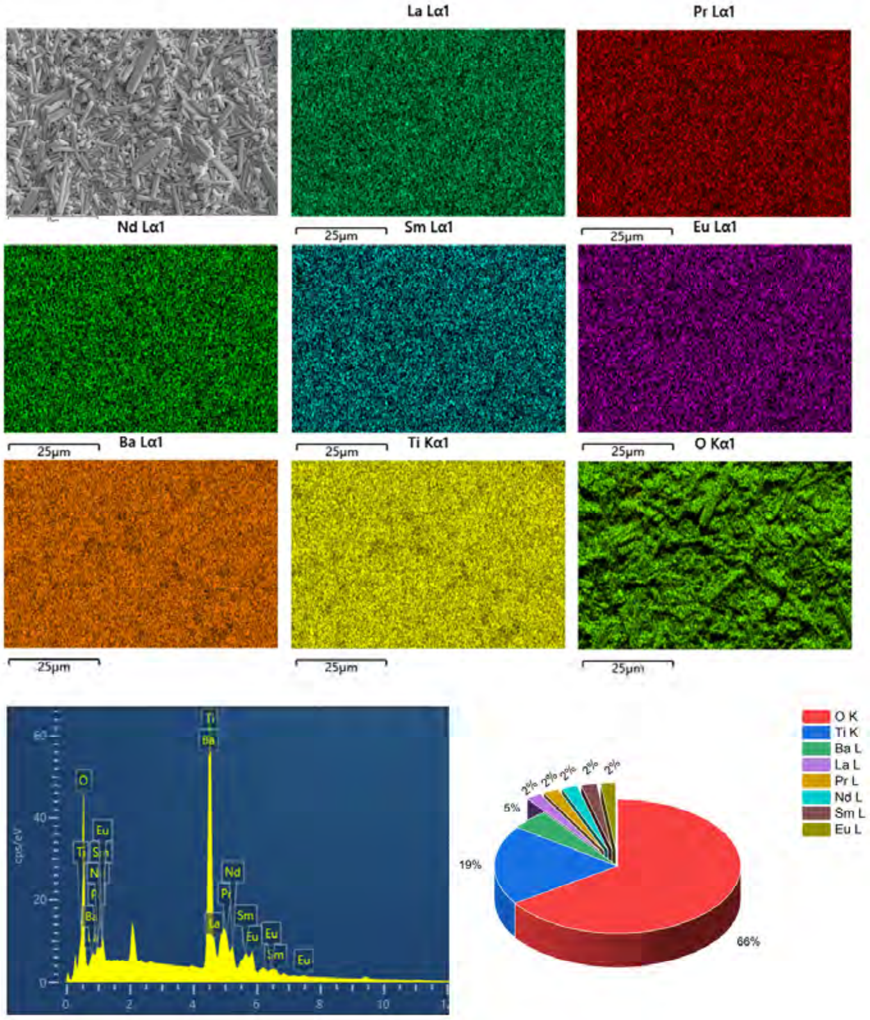

Figure 6. EDS mapping of BESNPLT HECs.

The measured ε_r and ρ_{re} of the BESNPLT HECs at varying temperatures (1350–1500 °C) are illustrated in Figure 7a. As the S.T. increased, the measured ε_r of the BESNPLT HECs exhibited an initial increase from 85.96 to 87.26, followed by a subsequent decrease to 82.68. The tendency for the measured ε_r of the BESNPLT HECs to align with that of ρ_{re} indicates that density played a pivotal role in determining permittivity. The polarizability per molar volume (α_{the}/V_m) and porosity-corrected permittivity (ε_{cor}) of the BESNPLT HECs are presented in Figure 7b. The ε_{cor} values were determined using Equation (3) [50]:

$$\varepsilon_{cor} = \varepsilon_r(1.5p + 1) \tag{3}$$

where p represents porosity determined from ρ_{re} ($p = 1 - \rho_{re}$). The α_{the}/V_m values were calculated using the Clausius–Mosotti formula, as outlined in Equation (4) [51]:

$$\frac{\alpha_{the}}{V_m} = \frac{3(\varepsilon_r - 1)}{4\pi(\varepsilon_r + 2)} \tag{4}$$

where V_m represents molar volume ($V_m = V/Z$, $Z = 2$ in BESNPLT HECs). The theoretical polarizability (α_{the}) of the BESNPLT HECs was determined using Equation (5) [51]:

$$\begin{gathered}\alpha_{\text{the}}(\text{BESNPLT}) = 4.5\alpha(\text{Ba}^{2+}) + 1.8\alpha(\text{La}^{3+}) + 1.8\alpha(\text{Pr}^{3+}) + 1.8(\text{Nd}^{3+}) + \\ 1.8\alpha(\text{Sm}^{3+}) + 1.8\alpha(\text{Eu}^{3+}) + 54\alpha(\text{O}^{2-}) + 18\alpha(\text{Ti}^{4+})\end{gathered} \tag{5}$$

where $\alpha(\text{Eu}^{3+})$ = 4.53 Å^3, $\alpha(\text{Sm}^{3+})$ = 4.74 Å^3, $\alpha(\text{Pr}^{3+})$ = 5.32 Å^3, $\alpha(\text{La}^{3+})$ = 6.07 Å^3, $\alpha(\text{Nd}^{3+})$ = 5.01 Å^3, $\alpha(\text{Ba}^{2+})$ = 6.4 Å^3, $\alpha(\text{O}^{2-})$ = 2.01 Å^3, and $\alpha(\text{Ti}^{4+})$ = 2.93 Å^3.

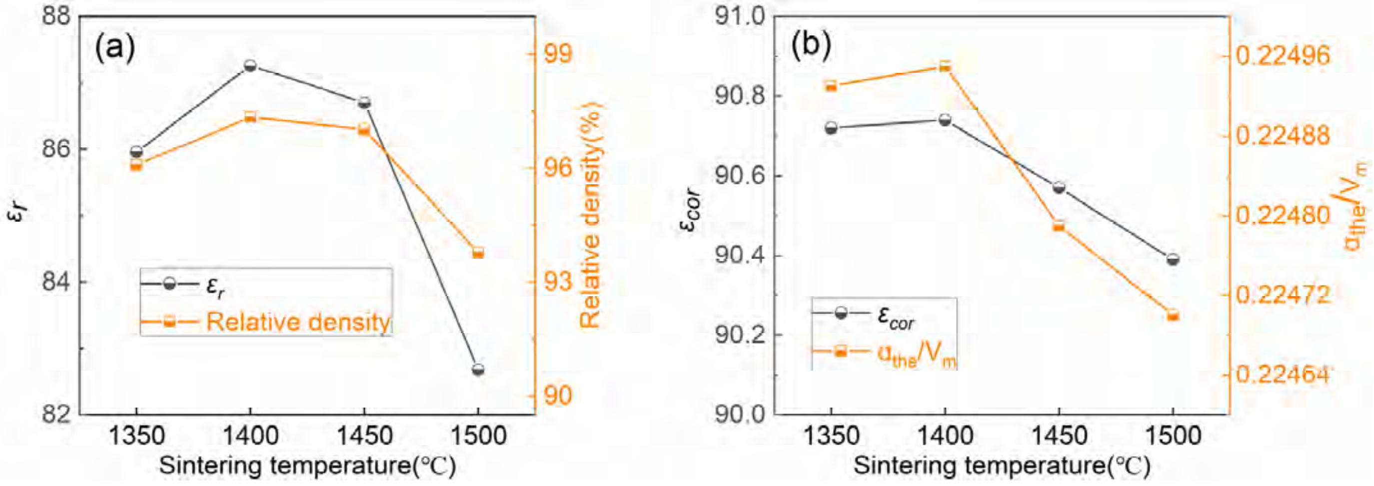

Figure 7. (**a**) ε_r and ρ_{re} of BESNPLT HECs; (**b**) ε_{cor} and α_{the}/V_m of BESNPLT HECs.

Furthermore, a direct proportional relationship was observed between ε_{cor} and α_{the}/V_m when the latter was considered as a single variable. As displayed in Figure 7b, α_{the}/V_m increases from 0.22493 (1350 °C) to 0.22495 (1400 °C) and then decreases to 0.2247 (1500 °C), explaining the change in the ε_{cor}. The results demonstrate that the key factors influencing the permittivity of the BESNPLT HECs are the α_{the}/V_m and density.

Figure 8a illustrates the $Q\times f$ and ρ_{re} of the BESNPLT HECs sintered at varying temperatures (1350–1500 °C). As presented in Figure 8a, $Q\times f$ demonstrates a slight increase from 7812 GHz to 8069 GHz as the S.T. rises from 1350 °C to 1400 °C. However, when the S.T. is further increased to 1500 °C, a notable reduction in the $Q\times f$ is observed. Dielectric loss ($tan\delta = 1/Q$) measured at the microwave band of ceramic materials is primarily influenced by intrinsic factors, including the lattice vibration, atomic packing fraction, and lattice energy, along with extrinsic factors such as microstructure, density, and lattice defects. A comparable trend was identified in the variation of $Q\times f$ in comparison to ρ_{re} (as illustrated in Figure 8a), implying that density had a significant impact on the $Q\times f$ values of the

BESNPLT HECs. In addition, the influence of the packing fraction (P.F.) on $Q{\times}f$ should be considered. The P.F. of the BESNPLT HECs could be determined through Equation (6) [52]:

$$\begin{aligned}\text{P.F.}(\%) &= \frac{\text{Packed ions volume}}{\text{Unit cell volume}} \times \mathrm{Z} \\ &= \frac{\frac{4\pi}{3}\left[4.5r_{Ba}^3+1.8(r_{Eu}^3+r_{Sm}^3+r_{Nd}^3+r_{\mathrm{Pr}}^3+r_{La}^3)+18r_{Ti}^3+54r_O^3\right]}{V} \times 2\end{aligned} \quad (6)$$

where r_{Ba} (1.52 Å), r_{Eu} (1.066 Å), r_{Sm} (1.079 Å), r_{Nd} (1.109 Å), r_{Pr} (1.126 Å), r_{La} (1.16 Å), r_O (1.4 Å), and r_{Ti} (0.605 Å) are ionic radii of the BESNPLT HECs. The increase in the P.F. of the microwave dielectric ceramics was found to be correlated with a reduction in lattice and non-harmonic vibration, which resulted in an enhancement of $Q{\times}f$. As illustrated in Figure 8b, the variation of $Q{\times}f$ for the BESNPLT HECs was aligned with that of the P.F. Therefore, the density and P.F are the key factors in determining the $Q{\times}f$ of the BESNPLT HECs.

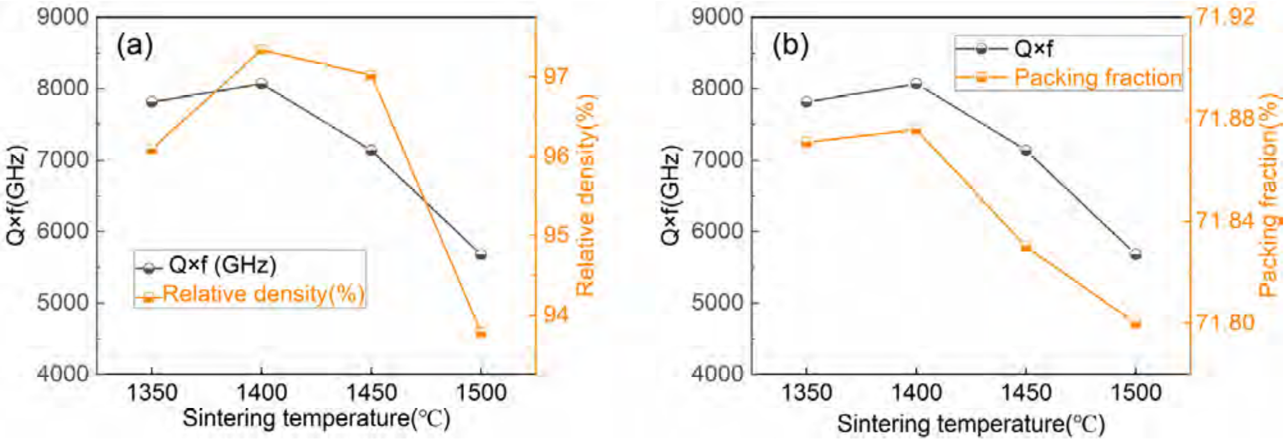

Figure 8. (**a**) $Q{\times}f$ and ρ_{re} of BESNPLT HECs; (**b**) $Q{\times}f$ and packing fraction of BESNPLT HECs.

In general, the TCF of the tungsten-bronze-type BRT (R represents the lanthanides) ceramics was found to be influenced by a number of factors, including the composition, the second phase, bond valence, and the tilt of Ti–O octahedron [53–55]. Figure 9a illustrates the TCF and B-site (Ti-site) bond valence (V_B) of the BESNPLT HECs as a function of the S.T. As the S.T. increased, the TCF of the BESNPLT HECs demonstrated a slight decrease from 39.7 to 38.9 ppm/°C, which was subsequently followed by an increase to 47.9 ppm/°C. The V_B of the BESNPLT HECs at varying temperatures (1350–1500 °C) is evaluated through Equations (7) and (8) [28]:

$$V_{jk} = \sum_k v_{jk} \quad (7)$$

$$v_{jk} = \exp\left[\frac{R_{jk} - d_{jk}}{0.37}\right] \quad (8)$$

where R_{jk} represents bond valence parameter, and d_{jk} denotes bond length. The decreasing degree of tilting on the Ti–O octahedron resulted in an increase in the TCF. Additionally, the degree of tilting observed in the Ti–O octahedron was influenced by the length and strength of the bonds between the oxygen and Ti-site cation. Accordingly, the degree of tilting on the Ti–O octahedron can be determined by the bond valence of the Ti-site cation, and the V_B of the BESNPLT HECs at varying temperatures demonstrated an inverse variation in the TCF, as illustrated in Figure 9a.

The tolerance factor (t) was found to be significantly correlated with the degree of tilting on the Ti–O octahedron in the tungsten-bronze-type BRT (R represents the lanthanides) MWDC. The t of the BESNPLT HECs could be determined using Equation (9):

$$t = \frac{[0.18\,(R_{Eu^{3+}} + R_{Sm^{3+}} + R_{Nd^{3+}} + R_{Pr^{3+}} + R_{La^{3+}}) + 0.1\,R_{Ba^{2+}}] + R_{O^{2-}}}{\sqrt{2}(R_{Ti^{4+}} + R_{O^{2-}})} \tag{9}$$

where R_{Ba}^{2+} (1.52 Å), R_{Eu}^{3+} (1.066 Å), R_{Sm}^{3+} (1.079 Å), R_{Nd}^{3+} (1.109 Å), R_{Pr}^{3+} (1.126 Å), R_{La}^{3+} (1.16 Å), R_{O}^{2-} (1.4 Å), and R_{Ti}^{4+} (0.605 Å) are the ionic radii of the BESNPLT HECs. Figure 9b presents the TCF and t of the $BaLa_2Ti_4O_{12}$ (BLT) [36], $BaPr_2Ti_4O_{12}$ (BPT) [56], $BaNd_2Ti_4O_{12}$ (BNT) [57], $BaSm_2Ti_4O_{12}$ (BST) [58], and BESNPLT ceramics. As t decreased, the degree of tilting on the Ti–O octahedron increased, resulting in a reduction in the TCF of the $BaR_2Ti_4O_{12}$ (R = lanthanides) ceramics. The TCF of the BESNPLT HECs could be adjusted to an appropriate value (+38.9 ppm/°C) through high-entropy design.

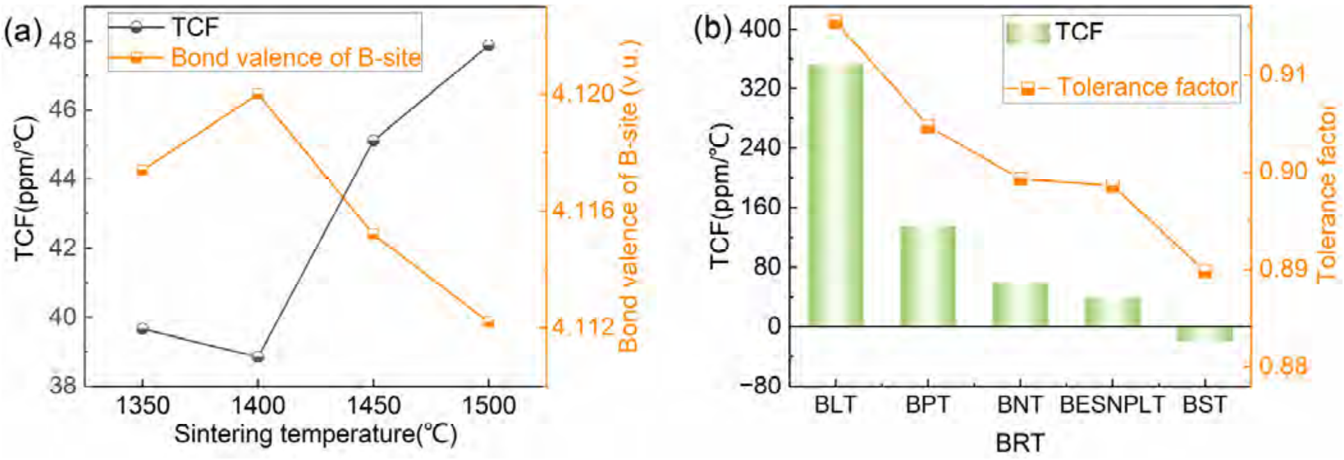

Figure 9. (**a**) TCF and B-site bond valence of BESNPLT HECs; (**b**) $BaLa_2Ti_4O_{12}$ (BLT) [36], $BaPr_2Ti_4O_{12}$ (BPT) [56], $BaNd_2Ti_4O_{12}$ (BNT) [57], $BaSm_2Ti_4O_{12}$ (BST) [58], and BESNPLT ceramics.

4. Conclusions

In this study, high-permittivity BESNPLT HECs were successfully produced using the concept of high entropy by a solid-phase reaction route. The results of the XRD and Raman analysis demonstrated that the BESNPLT HECs belonged to a single-phase tungsten-bronze-type structure with a Pnma space group within the S.T. range of 1350–1500 °C. The EDS mapping demonstrated that the distributions of the five lanthanide elements (Eu^{3+}, Sm^{3+}, Nd^{3+}, Pr^{3+}, and La^{3+}) were uniform in the BESNPLT HECs, confirming the formation of the BESNPLT solid solution. The microwave dielectric characteristics of the BESNPLT HECs were significantly influenced by a number of factors, including the polarizability, relative density, packing fraction, tolerance factor, and bond valence of the B-site (Ti-site). Specifically, the BESNPLT HECs achieved superior dielectric performances of TCF = +38.9 ppm/°C, $Q \times f$ = 8069 GHz (@6.1 GHz), and ε_r = 87.26. The present study has established a paradigm to optimize the dielectric characteristics of tungsten-bronze-type MWDC utilizing a high-entropy strategy.

Author Contributions: Conceptualization, Q.W. and G.W.; investigation, H.W. and Z.L.; methodology, Q.W.; supervision, Z.L.; validation, G.X.; writing—original draft, G.W.; writing—review and editing, H.W. and G.X. All authors have read and agreed to the published version of the manuscript.

Funding: The present work was supported by the Hubei Province Natural Science Foundation of China (2022CFB369), Hubei Province Department of Education Foundation (D20212803), and Ph.D. foundation (Grant No. BK202109).

Data Availability Statement: The original contributions presented in the study are included in the article; further inquiries can be directed to the corresponding author.

Conflicts of Interest: The authors declare no conflicts of interest.

References

1. Shehbaz, M.; Du, C.; Zhou, D.; Xia, S.; Xu, Z. Recent progress in dielectric resonator antenna: Materials, designs, fabrications, and their performance. *Appl. Phys. Rev.* **2023**, *10*, 021303. [CrossRef]
2. Du, K.; Zhou, M.; Li, C.; Yin, C.; Cai, Y.; Cheng, M.; Zhu, W.; Wei, G.; Wang, S.; Lei, W. Ultralow-Permittivity and Temperature-Stable $Ba_{1-x}Ca_xMg_2Al_6Si_9O_{30}$ Dielectric Ceramics for C-Band Patch Antenna Applications. *ACS Appl. Mater. Interfaces* **2024**, *16*, 23505–23516. [CrossRef]
3. Wang, W.; Wang, X.; Bao, J.; Jiang, J.; Fang, Z.; Jin, B.; Shi, Z.; Darwish, M.A.; Chen, Y.; Liang, Q.; et al. Low-permittivity $BaCuSi_4O_{10}$-based dielectric Ceramics: An available solution to connect low temperature cofired ceramic technology and millimeter-wave communications. *Chem. Eng. J.* **2024**, *494*, 153172. [CrossRef]
4. Sebastian, M.; Ubic, R.; Jantunen, H. Low-loss dielectric ceramic materials and their properties. *Int. Mater. Rev.* **2015**, *60*, 392–412. [CrossRef]
5. Xiang, H.; Zhang, Y.; Chen, J.; Zhou, Y.; Tang, Y.; Chen, J.; Fang, L. Structure evolution and τf influence mechanism of $Bi_{1-x}Ho_xVO_4$ microwave dielectric ceramics for LTCC applications. *J. Mater. Sci. Technol.* **2024**, *197*, 1–8. [CrossRef]
6. Wang, G.; Fu, Q.; Zha, L.; Hu, M.; Huang, J.; Zheng, Z.; Luo, W. Microwave dielectric characteristics of tungsten bronze-type $Ba_4Nd_{28/3}Ti_{18-y}Ga_{4y/3}O_{54}$ ceramics with temperature stable and ultra-low loss. *J. Eur. Ceram. Soc.* **2022**, *42*, 154–161. [CrossRef]
7. Tian, H.; Zhang, X.; Zhang, Z.; Liu, Y.; Wu, H. Low-permittivity $LiLn(PO_3)_4$ (Ln = La, Sm, Eu) dielectric ceramics for microwave/millimeter-wave communication. *J. Adv. Ceram.* **2024**, *13*, 602–620. [CrossRef]
8. Wang, G.; Zhang, D.; Huang, X.; Rao, Y.; Yang, Y.; Gan, G.; Lai, Y.; Xu, F.; Li, J.; Liao, Y. Crystal structure and enhanced microwave dielectric properties of Ta^{5+} substituted $Li_3Mg_2NbO_6$ ceramics. *J. Am. Ceram. Soc.* **2020**, *103*, 214–223.
9. Guo, W.; Lu, Y.; Ma, Z.; Wu, H.; Yue, Z. Defect-related broadband dielectric loss mechanisms of $Na_{1/2}Sm_{1/2}Ti_{1-z}(Al_{1/2}Nb_{1/2})_zO_3$ ceramics. *Acta Mater.* **2023**, *255*, 119093. [CrossRef]
10. Yao, G.; Zhao, J.; Lu, Y.; Liu, H.; Pei, C.; Ding, Q.; Chen, M.; Zhang, Y.; Li, D.; Wang, F. Microwave dielectric properties of Li_3TiO_3F oxyfluorides ceramics. *Crystals* **2023**, *13*, 897. [CrossRef]
11. Ma, L.; Tian, G.; Xiao, H.; Jiang, L.; Du, Q.; Li, H.; Yang, B. A novel spinel-type $Mg_3Ga_2SnO_8$ microwave dielectric ceramic with low ε and low loss. *J. Eur. Ceram. Soc.* **2024**, *44*, 5731–5737. [CrossRef]
12. Oses, C.; Toher, C.; Curtarolo, S. High-entropy ceramics. *Nat. Rev. Mater.* **2020**, *5*, 295–309. [CrossRef]
13. Xiang, H.; Xing, Y.; Dai, F.-z.; Wang, H.; Su, L.; Miao, L.; Zhang, G.; Wang, Y.; Qi, X.; Yao, L. High-entropy ceramics: Present status, challenges, and a look forward. *J. Adv. Ceram.* **2021**, *10*, 385–441. [CrossRef]
14. Akrami, S.; Edalati, P.; Fuji, M.; Edalati, K. High-entropy ceramics: Review of principles, production and applications. *Mater. Sci. Eng. R Rep.* **2021**, *146*, 100644. [CrossRef]
15. Anandkumar, M.; Trofimov, E. Synthesis, properties, and applications of high-entropy oxide ceramics: Current progress and future perspectives. *J. Alloy. Compd.* **2023**, *960*, 170690. [CrossRef]
16. Jiao, Y.; Dai, J.; Fan, Z.; Cheng, J.; Zheng, G.; Grema, L.; Zhong, J.; Li, H.-F.; Wang, D. Overview of high-entropy oxide ceramics. *Mater. Today* **2024**, *77*, 92–117. [CrossRef]
17. Banerjee, R.; Chatterjee, S.; Ranjan, M.; Bhattacharya, T.; Mukherjee, S.; Jana, S.S.; Dwivedi, A.; Maiti, T. High-entropy perovskites: An emergent class of oxide thermoelectrics with ultralow thermal conductivity. *ACS Sustain. Chem. Eng.* **2020**, *8*, 17022–17032. [CrossRef]
18. Harrington, T.J.; Gild, J.; Sarker, P.; Toher, C.; Rost, C.M.; Dippo, O.F.; McElfresh, C.; Kaufmann, K.; Marin, E.; Borowski, L. Phase stability and mechanical properties of novel high entropy transition metal carbides. *Acta Mater.* **2019**, *166*, 271–280. [CrossRef]
19. Zhou, S.; Pu, Y.; Zhang, Q.; Shi, R.; Guo, X.; Wang, W.; Ji, J.; Wei, T.; Ouyang, T. Microstructure and dielectric properties of high entropy $Ba(Zr_{0.2}Ti_{0.2}Sn_{0.2}Hf_{0.2}Me_{0.2})O_3$ perovskite oxides. *Ceram. Int.* **2020**, *46*, 7430–7437. [CrossRef]
20. Li, H.; Zhao, J.; Li, Y.; Chen, L.; Chen, X.; Qin, H.; Zhou, H.; Li, P.; Guo, J.; Wang, D. Bismuth Ferrite-Based Lead-Free High-Entropy Piezoelectric Ceramics. *ACS Appl. Mater. Interfaces* **2024**, *16*, 9078–9087. [CrossRef]
21. Zhang, M.; Xu, X.; Ahmed, S.; Yue, Y.; Palma, M.; Svec, P.; Gao, F.; Abrahams, I.; Reece, M.J.; Yan, H. Phase transformations in an Aurivillius layer structured ferroelectric designed using the high entropy concept. *Acta Mater.* **2022**, *229*, 117815. [CrossRef]
22. von Fieandt, K.; Paschalidou, E.-M.; Srinath, A.; Soucek, P.; Riekehr, L.; Nyholm, L.; Lewin, E. Multi-component (Al, Cr, Nb, Y, Zr) N thin films by reactive magnetron sputter deposition for increased hardness and corrosion resistance. *Thin Solid Film* **2020**, *693*, 137685. [CrossRef]
23. Liu, Y.; Yang, J.; Deng, S.; Zhang, Y.; Zhang, Y.; Sun, S.; Wang, L.; Jiang, X.; Huo, C.; Liu, H. Flexible polarization configuration in high-entropy piezoelectrics with high performance. *Acta Mater.* **2022**, *236*, 118115. [CrossRef]
24. Ren, K.; Wang, Q.; Shao, G.; Zhao, X.; Wang, Y. Multicomponent high-entropy zirconates with comprehensive properties for advanced thermal barrier coating. *Scr. Mater.* **2020**, *178*, 382–386. [CrossRef]
25. Guo, J.; Yu, H.; Ren, Y.; Qi, H.; Yang, X.; Deng, Y.; Zhang, S.-T.; Chen, J. Multi-symmetry high-entropy relaxor ferroelectric with giant capacitive energy storage. *Nano Energy* **2023**, *112*, 108458. [CrossRef]

26. Xiang, H.; Yao, L.; Chen, J.; Yang, A.; Yang, H.; Fang, L. Microwave dielectric high-entropy ceramic $Li(Gd_{0.2}Ho_{0.2}Er_{0.2}Yb_{0.2}Lu_{0.2})GeO_4$ with stable temperature coefficient for low-temperature cofired ceramic technologies. *J. Mater. Sci. Technol.* **2021**, *93*, 28–32. [CrossRef]
27. Ding, Y.H.; Liu, L.; Guo, R.Z.; Li, L.; Chen, X.M. $(Hf_{0.25}Zr_{0.25}Sn_{0.25}Ti_{0.25})O_2$ high-entropy ceramics and their microwave dielectric characteristics. *J. Am. Ceram. Soc.* **2022**, *105*, 6710–6717. [CrossRef]
28. Lin, F.L.; Liu, B.; Hu, C.C.; Song, K.X. Novel high-entropy microwave dielectric ceramics $Sr(La_{0.2}Nd_{0.2}Sm_{0.2}Eu_{0.2}Gd_{0.2})AlO_4$ with excellent temperature stability and mechanical properties. *J. Eur. Ceram. Soc.* **2023**, *43*, 2506–2512. [CrossRef]
29. Xie, M.; Li, X.; Lai, Y.; Qi, C.; Yin, J.; Gong, W.; Li, Y.; Liu, Q.; Wu, C. Phase evolution and microware dielectric properties of high-entropy spinel-type $(Mg_{0.2}Co_{0.2}Ni_{0.2}Li_{0.4}Zn_{0.2})Al_2O_4$ ceramics. *J. Eur. Ceram. Soc.* **2024**, *44*, 284–292. [CrossRef]
30. Chen, D.; Yan, N.; Cao, X.; Li, F.; Liu, L.; Shen, Q.; Zhou, H.; Li, C. Entropy regulation in $LaNbO_4$-based fergusonite to implement high-temperature phase transition and promising dielectric properties. *J. Adv. Ceram.* **2023**, *12*, 1067–1080. [CrossRef]
31. Huanrong, T.; Zhang, X.; Du, W.; Feng, Z.; Wang, L.; Haitao, W.; Xia, W. Structure characteristics and microwave/terahertz dielectric response of low-permittivity $(La_{0.2}Nd_{0.2}Sm_{0.2}Eu_{0.2}Gd_{0.2})_2Zr_3(Mo\ O_4)_9$ high-entropy ceramics. *Ceram. Int.* **2024**, *50*, 6403–6411.
32. Xiao, L.; Deng, L.; Li, Y.; Qing, Z.; Xi, Y.; Zhu, J.; Peng, S. A $TiSnNbTaGa_2O_{12}$ high-entropy microwave dielectric ceramic with rutile structure and near-zero τf. *J. Eur. Ceram. Soc.* **2024**, *44*, 277–283. [CrossRef]
33. Chen, D.; Zhu, X.; Xiong, S.; Zhu, G.; Liu, L.; Khaliq, J.; Li, C. Tunable Microwave Dielectric Properties in Rare-Earth Niobates via a High-Entropy Configuration Strategy to Induce Ferroelastic Phase Transition. *ACS Appl. Mater. Interfaces* **2023**, *15*, 52776–52787. [CrossRef]
34. Liu, K.; Zhang, H.; Liu, C.; Li, J.; Shi, L.; Wang, X.; Zhang, D. Crystal structure and microwave dielectric properties of $(Mg_{0.2}Ni_{0.2}Zn_{0.2}Co_{0.2}Mn_{0.2})_2SiO_4$-A novel high-entropy ceramic. *Ceram. Int.* **2022**, *48*, 23307–23313. [CrossRef]
35. Du, Q.; Duan, J.; Ma, L.; Jiang, L.; Li, H. Sintering temperature, microwave dielectric properties and structural characteristics of $Li_2Zn_6MgTi_6O_{20}$ ceramic with high configuration entropy. *J. Eur. Ceram. Soc.* **2024**, *44*, 5639–5645. [CrossRef]
36. Muhammad, R.; Iqbal, Y.; Rambo, C.R. Characterization of $Ba_{4.5}Re_9Ti_{18}O_{54}$ (Re = La, Nd) microwave dielectric ceramics. *J. Mater. Sci. Mater. Electron.* **2014**, *25*, 1652–1656. [CrossRef]
37. Hakki, B.; Coleman, P.D. A dielectric resonator method of measuring inductive capacities in the millimeter range. *IRE Trans. Microw. Theory Tech.* **1960**, *8*, 402–410. [CrossRef]
38. Shannon, R.D. Revised effective ionic radii and systematic studies of interatomic distances in halides and chalcogenides. *Acta Crystallogr. Sect. A Cryst. Phys. Diffr. Theor. Gen. Crystallogr.* **1976**, *32*, 751–767. [CrossRef]
39. Rietveld, H.M. A profile refinement method for nuclear and magnetic structures. *J. Appl. Crystallogr.* **1969**, *2*, 65–71. [CrossRef]
40. Toby, B.H. EXPGUI, a graphical user interface for GSAS. *J. Appl. Crystallogr.* **2001**, *34*, 210–213. [CrossRef]
41. Tang, C.; Roberts, M.; Azough, F.; Leach, C.; Freer, R. Synchrotron X-ray diffraction study of $Ba_{4.5}Nd_9Ti_{18}O_{54}$ microwave dielectric ceramics at 10–295 K. *J. Mater. Res.* **2002**, *17*, 675–682. [CrossRef]
42. Ohsato, H. Science of tungstenbronze-type like $Ba_{6-3x}R_{8+2x}Ti_{18}O_{54}$ (R = rare earth) microwave dielectric solid solutions. *J. Eur. Ceram. Soc.* **2001**, *21*, 2703–2711. [CrossRef]
43. Hao, S.Z.; Zhou, D.; Pang, L.X. The spectra analysis and microwave dielectric properties of $[Ca_{0.55}(Sm_{1-x}Bi_x)_{0.3}]MoO_4$ ceramics. *J. Am. Ceram. Soc.* **2019**, *102*, 3103–3109. [CrossRef]
44. Li, L.; Wang, X.; Luo, W.; Wang, S.; Yang, T.; Zhou, J. Internal-strain-controlled tungsten bronze structural ceramics for 5G millimeter-wave metamaterials. *J. Mater. Chem. C* **2021**, *9*, 14359–14370. [CrossRef]
45. Ning, F.; Lin, G.; Yuan, S.; Qi, Z.; Jiang, J.; Zhang, T. Correlation between vibrational modes of A-site ions and microwave dielectric properties in $(1-x)CaTiO_3-x(Li_{0.5}Sm_{0.5})TiO_3$ ceramics. *J. Alloys Comp.* **2017**, *729*, 742–748. [CrossRef]
46. Guo, W.; Ma, Z.; Luo, Y.; Chen, Y.; Yue, Z.; Li, L. Structure, defects, and microwave dielectric properties of Al-doped and Al/Nd co-doped $Ba_4Nd_{9.33}Ti_{18}O_{54}$ ceramics. *J. Adv. Ceram.* **2022**, *11*, 629–640. [CrossRef]
47. Wang, G.; Fu, Q.; Guo, P.; Hu, M.; Wang, H.; Yu, S.; Zheng, Z.; Luo, W. Crystal structure, spectra analysis and dielectric characteristics of $Ba_4M_{28/3}Ti_{18}O_{54}$ (M = La, Pr, Nd, and Sm) microwave ceramics. *Ceram. Int.* **2021**, *47*, 1750–1757. [CrossRef]
48. Luo, W.; Wang, X.; Bai, B.; Qiao, J.; Chen, X.; Wen, Y.; Sun, J.; Li, L.; Zhou, J. B-site internal-strain regulation engineering of tungsten bronze structural dielectric ceramics. *J. Am. Ceram. Soc.* **2024**, *107*, 367–376. [CrossRef]
49. Guo, W.; Yang, Y.; Ma, Z.; Lu, Y.; Yue, Z. Effects of Zr^{4+} and Hf^{4+} substitution on the structure and dielectric response of $Ba_4Sm_{9.\ 33}Ti_{18}O_{54}$ ceramics. *Ceram. Int.* **2024**, *50*, 12443–12449. [CrossRef]
50. Penn, S.J.; Alford, N.M.; Templeton, A.; Wang, X.; Xu, M.; Reece, M.; Schrapel, K. Effect of porosity and grain size on the microwave dielectric properties of sintered alumina. *J. Am. Ceram. Soc.* **1997**, *80*, 1885–1888. [CrossRef]
51. Shannon, R.D. Dielectric polarizabilities of ions in oxides and fluorides. *J. Appl. Phys.* **1993**, *73*, 348–366. [CrossRef]
52. Kim, E.S.; Chun, B.S.; Freer, R.; Cernik, R.J. Effects of packing fraction and bond valence on microwave dielectric properties of $A^{2+}B^{6+}O_4$ (A^{2+}: Ca, Pb, Ba; B^{6+}: Mo, W) ceramics. *J. Eur. Ceram. Soc.* **2010**, *30*, 1731–1736. [CrossRef]
53. Ubic, R.; Reaney, I.; Lee, W. Microwave dielectric solid–solution phase in system $BaO-Ln_2O_3-TiO_2$ (Ln = lanthanide cation). *Int. Mater. Rev.* **1998**, *43*, 205–219. [CrossRef]
54. Xiong, Z.; Tang, B.; Fang, Z.; Yang, C.; Zhang, S. Crystal structure, Raman spectroscopy and microwave dielectric properties of $Ba_{3.75}Nd_{9.5}Ti1_{8-z}(Al_{1/2}Nb_{1/2})_zO_{54}$ ceramics. *J. Alloys Compd.* **2017**, *723*, 580–588. [CrossRef]

55. Wang, G.; Fu, Q.; Shi, H.; Tian, F.; Guo, P.; Yan, L.; Yu, S.; Zheng, Z.; Luo, W. Novel thermally stable, high quality factor $Ba_4(Pr_{0.4}Sm_{0.6})_{28/3}Ti_{18-y}Ga_{4y/3}O_{54}$ microwave dielectric ceramics. *J. Am. Ceram. Soc.* **2020**, *103*, 2520–2527. [CrossRef]
56. Solomon, S.; Santha, N.; Jawahar, I.; Sreemoolanadhan, H.; Sebastian, M.; Mohanan, P. Tailoring the microwave dielectric properties of $BaRE_2Ti_4O_{12}$ and $BaRE_2Ti_5O_{14}$ ceramics by compositional variations. *J. Mater. Sci. Mater. Electron.* **2000**, *11*, 595–602. [CrossRef]
57. Ubic, R.; Reaney, I.M.; Lee, W.E.; Samuels, J.; Evangelinos, E. Properties of the microwave dielectric phase $Ba_{6-3X}Nd_{8+2X}Ti_{18}O_{54}$. *Ferroelectrics* **1999**, *228*, 271–282. [CrossRef]
58. Cheng, P.-S.; Yang, C.-F.; Chen, Y.-C.; Tzou, W.-C. The reaction sequence and dielectric properties of $BaSm_2Ti_4O_{12}$ ceramics. *Ceram. Int.* **2000**, *26*, 877–881. [CrossRef]